


RESEARCH

Open Access



In-situ TiO_{2-x} decoration of titanium carbide MXene for photo/sono-responsive antitumor theranostics

Dong-Yang Zhang^{1,2†}, Hengke Liu^{2†}, Muhammad Rizwan Younis^{2†}, Shan Lei², Yunzhi Chen¹, Peng Huang^{2*}  and Jing Lin^{1,2*}

Abstract

Background: Sonodynamic therapy (SDT) has emerged as a noninvasive therapeutic modality that involves sonosensitizers and low-intensity ultrasound. However, owing to the rapid recombination of charge carriers, most of the sonosensitizers triggered poor reactive oxygen species (ROS) generation, resulting in unsatisfactory sonodynamic therapeutic effects.

Results: Herein, a photo/sono-responsive nanoplatform was developed through the *in-situ* synthesis of TiO_{2-x} on the surface of two-dimensional MXene (titanium carbide, Ti₃C₂) for photoacoustic/photothermal bimodal imaging-guided near-infrared II (NIR-II) photothermal enhanced SDT of tumor. Because of several oxygen vacancies and smaller size (~10 nm), the *in-situ* formed TiO_{2-x} nanoparticles possessed narrow band gap (2.65 eV) and high surface area, and thus served as a charge trap to restrict charge recombination under ultrasound (US) activation, resulting in enhanced sonodynamic ROS generation. Moreover, Ti₃C₂ nanosheets induced extensive localized hyperthermia relieves tumor hypoxia by accelerating intratumoral blood flow and tumor oxygenation, and thus further strengthened the efficacy of SDT. Upon US/NIR-II laser dual-stimuli, Ti₃C₂@TiO_{2-x} nanoplatform triggered substantial cellular killing *in vitro* and complete tumor eradication *in vivo*, without any tumor recurrence and systemic toxicity.

Conclusion: Our work presents the promising design of photo/sono-responsive nanoplatform for cancer nanotheranostics.

Keywords: Titanium carbide, Oxygen deficient titanium dioxide, Photoacoustic imaging, Photothermal therapy, Sonodynamic therapy

*Correspondence: peng.huang@szu.edu.cn; jingl@szu.edu.cn

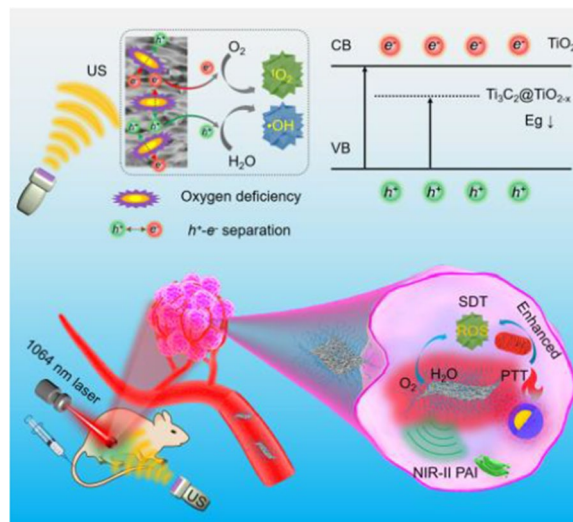
[†]Dong-Yang Zhang, Hengke Liu and Muhammad Rizwan Younis contributed equally to this work

¹ Department of Hepatobiliary Surgery, The First Affiliated Hospital of Wenzhou Medical University Wenzhou, Zhejiang 325000, China

² International Cancer Center, Laboratory of Evolutionary Theranostics (LET), School of Biomedical Engineering, Marshall Laboratory of Biomedical Engineering, Shenzhen University Health Science Center, Shenzhen 518060, China



Graphical Abstract

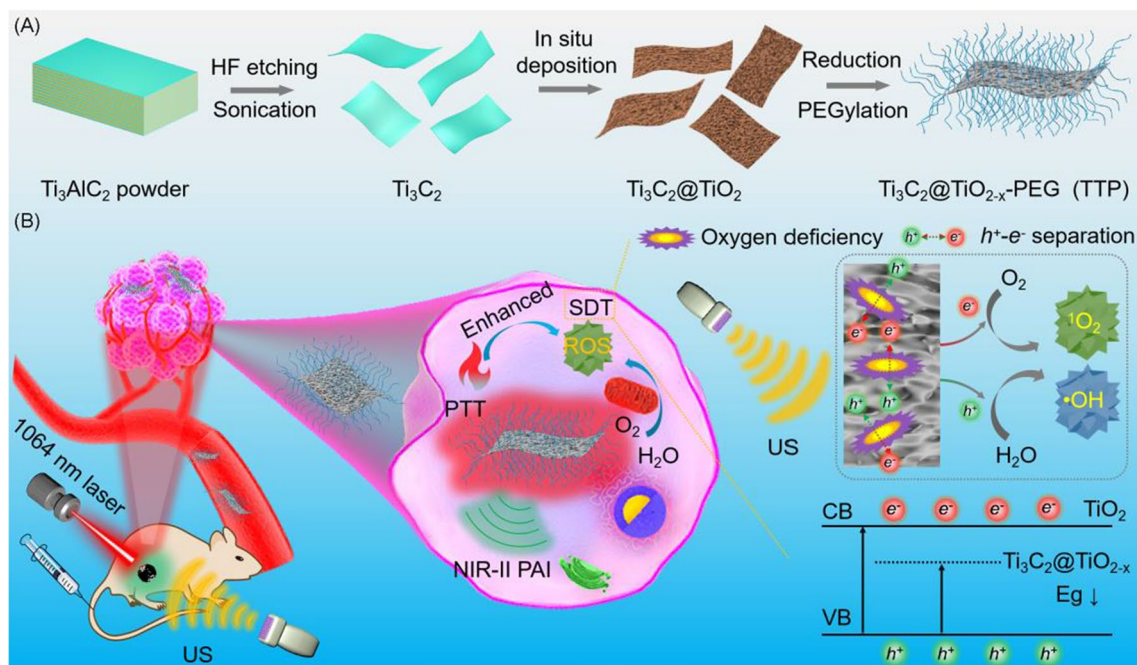


Introduction

Sonodynamic therapy (SDT), a type of non-invasive tumor modality, offered promising advantages than conventional tumor treatment, such as high tissue penetration, high spatiotemporal selectivity, and non-invasiveness [1–6]. In SDT, sonosensitizers triggered reactive oxygen species (ROS) production under ultrasound (US) stimulation, leading to selective tumor cell killing with minimal damage to nearby healthy cells [7–11]. Hence, several organic and inorganic sonosensitizers have been developed, however, organic sonosensitizers are mainly suffer from high skin phototoxicity [12, 13]. Alternatively, inorganic sonosensitizers with negligible phototoxicity and enhanced chemical stability, respectively, have shown great promise for tumor SDT. Especially, titanium dioxide (TiO_2) as an inorganic sonosensitizer, has been widely employed, but the rapid recombination (50 ± 30 ns) of US-mediated charge carriers (electron–hole pair) endows TiO_2 with poor ROS quantum yield, resulting in limited SDT efficacy [14]. Previous reports suggested that the presence of oxygen deficiencies within TiO_2 or the integration of TiO_2 with noble metals could improve the SDT activity [15–18], however, because of the large size TiO_2 NPs, the adsorption of oxygen molecules onto the surface of TiO_2 is remarkably poor, leading to unsatisfactory ROS yield. Thus, an optimal design engineering of inorganic sonosensitizers is desirable to overcome these limitations, promoting high SDT performance under US activation. Moreover, as the SDT reaction is exclusively dependent on tissues oxygen, the continuous sonodynamic ROS generation induced severe tumor hypoxia due to oxygen depletion, and hence, restricts the overall

SDT efficacy. Therefore, the integration of SDT with other non-invasive tumor treatment modalities, which may complement SDT effects, is greatly needed.

Being activated by an external light source, photothermal therapy (PTT) is an ideal non-invasive treatment modality, which induced irreversible destruction of tumor cells via localized hyperthermia generated by photothermal agents [19–22]. As photothermal agents with NIR-I light absorption have been actively developed, NIR-I tumor PTT is well-established, while PTT of deep-seated tumors at second biowindow (NIR-II) is yet limited. Moreover, though NIR-I laser light excitation endows PTT with sufficient penetration depth, an inhomogeneous thermal distribution as well as tumor self-regulation limit the complete photothermal eradication of deep-seated tumors, favoring tumor recurrence and metastasis [23]. Previously, Xia et al. demonstrated photothermal enhanced photodynamic therapy (PDT) of HeLa tumor in vivo under low power single NIR-I laser activation [24]. They suggested that localized hyperthermia could not only activate PDT by the controlled release of indocyanine green, but also relieve PDT-induced tumor hypoxia, leading to accelerate photodynamic tumor killing. Recently, our group have shown that PTT under both NIR-I and NIR-II laser excitation, could enhance multimodal tumor therapies such as starvation therapy, chemodynamic therapy, and immunotherapy [25–28]. Notably, it has been reported that PTT could complement SDT as mild hyperthermia accelerates intratumoral blood flow and tumor oxygenation, which promote sonodynamic ROS generation by relieving tumor hypoxia [29–31]. Whereas, under US activation, SDT



Scheme 1 Schematic illustration of **A** the preparation of *in-situ* fabricated TTP nanohybrids and **B** their application in bimodal PA/PT imaging guided synergistic photothermal-enhanced sonodynamic therapy in NIR-II biowindow

also complements PTT by ROS-mediated tumor cell killing as well as replenishment of thermally resistant deeply localized tumors due to the high penetration depth of US [32]. Considering the prominent features of individual PTT and SDT, their integration would be highly advantageous to overcome their inherent limitations and achieve ultimate therapeutic effects.

Two-dimensional MXene nanomaterials, such as titanium carbide (Ti_3C_2), are widely used in biomedical applications [33–40]. Particularly, Ti_3C_2 with good absorption in NIR-II region, excellent photothermal performance, and low toxicity, has become a potential photothermal therapeutic agent. Furthermore, multimodal imaging capacity of Ti_3C_2 provides an opportunity to monitor nanomaterials biodistribution as well as effectively guide the tumor treatment *in vivo*. Owing to the promising biomedical characteristics, Ti_3C_2 is an ideal candidate to couple with sonosensitizer to trigger PTT enhanced SDT of deep-seated tumors at second biowindow. In this study, a Ti_3C_2 -based 2D nanotheranostic hybrid is constructed *in-situ* for duplex photoacoustic (PA)/photothermal imaging-guided synergistic PTT/enhanced SDT at NIR-II biowindow (Scheme 1). In brief, the multifunctional nanohybrid ($\text{Ti}_3\text{C}_2@\text{TiO}_{2-x}$) is developed by a hydrothermal method via *in-situ* growth of TiO_{2-x} nanoparticles with several oxygen defects onto Ti_3C_2 nanosheets. The resultant $\text{Ti}_3\text{C}_2@\text{TiO}_{2-x}$

were further modified with polyethylene glycol (PEG), defined as TTP, showing good biocompatibility and aqueous dispersibility in various physiological solutions. The as-obtained TTP not only exhibits good photothermal performance, but also demonstrates superior ROS production under US excitation than TiO_2 due to high surface area and the presence of multiple oxygen vacancies, promoting enhanced separation of charge carriers (electron–hole pairs). A remarkably higher therapeutic efficacy was achieved under dual-modal PA/PT imaging guidance both *in vitro* and *in vivo*, without any obvious toxic effects after intravenous administration. This study provides a promising strategy of photo-sonoinduced theranostics of deeply localized tumors.

Material and methods

Preparation of $\text{Ti}_3\text{C}_2@\text{TiO}_{2-x}$ -PEG (TTP)

Ti_3C_2 nanosheets were obtained following the reported literature [36]. Then, 2D $\text{Ti}_3\text{C}_2@\text{TiO}_2$ hybrid was fabricated according to the previous report with slight modification. 100 mg of Ti_3C_2 was dispersed in 3.0 M hydrochloric acid (15 mL) containing 0.04 M ammonium fluoride. Above dispersion was transferred to the Teflon stainless steel autoclave and kept at 200 °C for 12 h. After centrifugation and washing with deionized (DI) water, the as-collected $\text{Ti}_3\text{C}_2@\text{TiO}_2$ precipitate was added to hydrazine hydrate solution (25 mL, 50 wt%) under

stirring. Next, the suspension was further transferred to the Teflon stainless steel autoclave and kept at 200 °C for 12 h. The final $\text{Ti}_3\text{C}_2@\text{TiO}_{2-x}$ hybrid was obtained by centrifugation and washing with DI water.

To improve the solubility and biocompatibility of $\text{Ti}_3\text{C}_2@\text{TiO}_{2-x}$, 20 mg of DSPE-PEG dissolved in chloroform (20 mL) was added dropwise into $\text{Ti}_3\text{C}_2@\text{TiO}_{2-x}$ ethanol solution (2 mg/mL, 20 mL) under ultrasonication. The product was obtained by evaporating the solvent and then resuspended in phosphate buffered saline (PBS), and finally stored at 4 °C for future use.

In vivo toxicity

BALB/c female mice ($n \geq 3$) were intravenously (*i.v.*) injected with TTP nanohybrids (4 mg/mL, 200 μL) or PBS (200 μL). The body weight of mice was recorded every 3 days. The blood and primary organs (kidneys, lungs, spleen, liver, heart) were acquired after 30 days post-injection. The blood was used to perform hematologic analysis and the primary organs were stained by hematoxylin and eosin (H&E). All animal experiments were conducted as per the approved institutional guidelines for the care of laboratory animals of Shenzhen University.

Photoacoustic/thermal imaging and biodistribution of nanohybrids in vivo

PA signals of the varying concentrations of TTP nanohybrid in solution were recorded by a photoacoustic imager. For *in vivo* NIR-II PA imaging, 4T1 tumor-bearing mice ($n=3$) were *i.v.* injected with TTP nanohybrids (2 mg/mL, 200 μL), and the PA signals were monitored at different time points (0, 1, 2, 4, 8, and 24 h).

4T1 tumor-bearing BALB/c nude mice were *i.v.* injected with TTP nanohybrid (2 mg/mL, 200 μL). After 4 h post-injection, the tumors were irradiated by a 1064 nm laser and the real-time temperature changes were monitored with a thermal imager.

4T1 tumor-bearing nude mice ($n=3$) were *i.v.* injected with TTP nanohybrid (2 mg/mL, 200 μL). After 24 h post-injection, the mice were euthanized to collect the primary organs. The primary organs were digested by aqua regia and determined by ICP-MS. The biodistribution of Ti (% ID of Ti per gram of tissues) was calculated in primary organs.

In vivo treatment

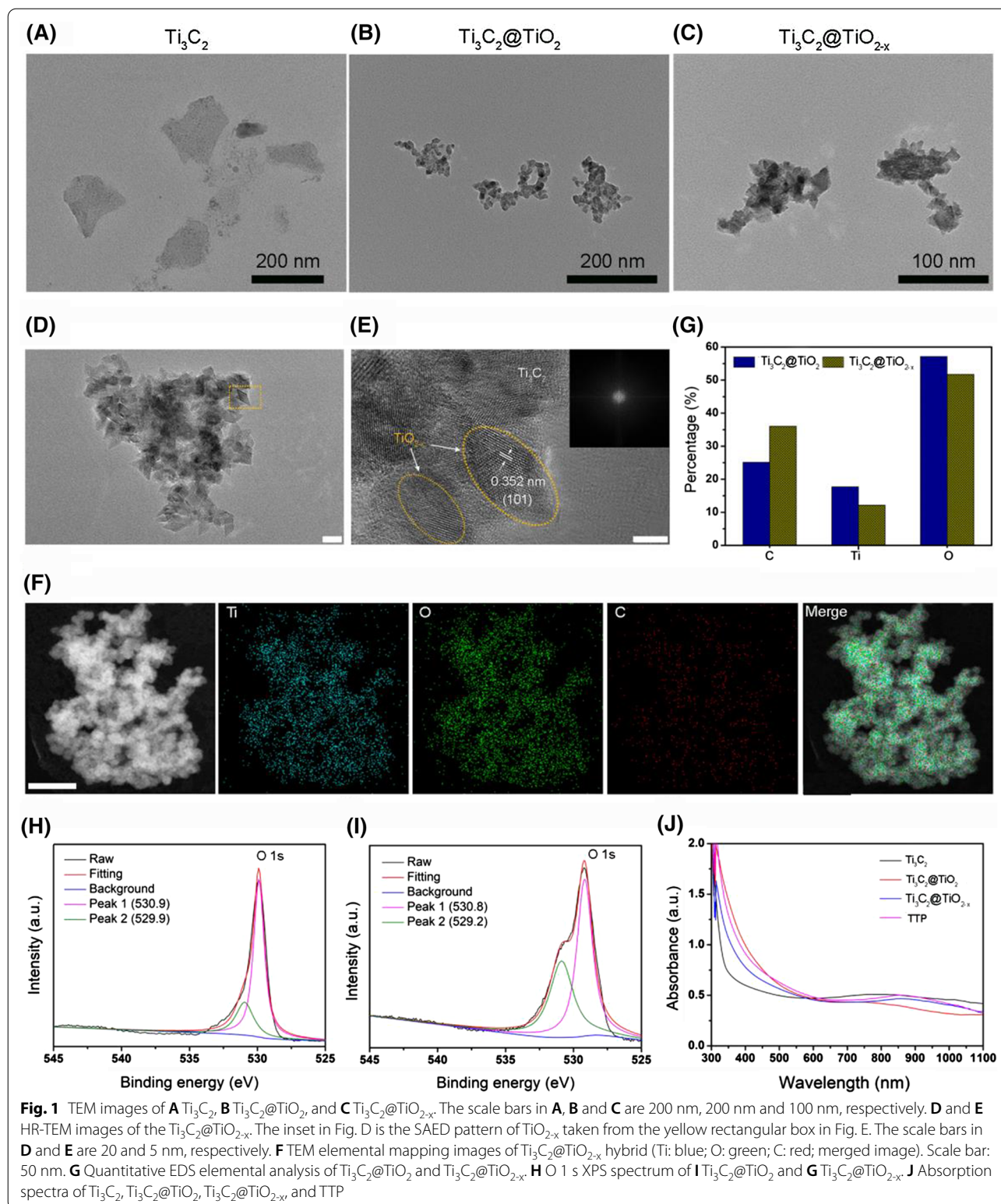
4T1 tumor-bearing BALB/c nude mice with $\sim 50 \text{ mm}^3$ tumor volume, were randomly divided into 6 groups ($n \geq 5$) as follows: (i) PBS, (ii) laser + US (iii) TTP nanohybrid, (iv) TTP nanohybrid + US, (v) TTP nanohybrid + laser, (vi) TTP nanohybrid + laser + US. After 4 h post-injection, the tumors were treated with laser

irradiation (1064 nm, 0.8 W/cm^2 , 10 min) or/and US (1 W/cm^2 , 5 min). The tumor volumes and body weights of mice were recorded every 2 days. The tumor volume was calculated based on the formula: $V (\text{mm}^3) = AB^2/2$, where A and B are the maximum length (mm) and the minimum width (mm) of the tumor, respectively. The body weights of mice were recorded every 2 days. The mice were sacrificed at 14th day post-treatment to collect tumors, serum, and primary organs. The tumors were photographed, weighed, and stained by Terminal-deoxynucleotidyl transferase mediated nick end labeling (TUNEL) assay. The serum was used to determine the levels of liver and kidney function indicators, while the primary organs and tumor were stained by H&E for histopathological investigations.

Results and discussion

Synthesis and characterization

The development of TTP nanohybrid was carried out in several steps. In brief, bulk Ti_3C_2 powder was first exfoliated via ultrasonication by using TPAOH as an intercalating agent, resulting in the formation of 2D Ti_3C_2 nanosheets with an approximate lateral dimension of 150 nm (Fig. 1A). Next, TiO_2 NPs were grown in situ onto the as-obtained 2D Ti_3C_2 nanosheets by hydrothermal method [41]. Compared to the usually prepared TiO_2 NPs ($\sim 100 \text{ nm}$) [15, 42, 43], in situ fabricated TiO_2 NPs were much smaller ($\sim 10 \text{ nm}$) in diameter as revealed by TEM (Fig. 1B). Considering an inverse relationship between the NPs size and their surface area, the as-obtained TiO_2 NPs with high surface area could facilitate higher surface adsorption of oxygen molecules and the separation of electron-hole pairs, promoting higher ROS generation [44, 45]. Finally, an engineering of *in-situ* developed $\text{Ti}_3\text{C}_2@\text{TiO}_2$ was performed through hydrazine hydrate reduction method [46], which induced multiple oxygen defects within TiO_2 NPs, resulting in the formation of $\text{Ti}_3\text{C}_2@\text{TiO}_{2-x}$ nanohybrid. Notably, no apparent aggregation or morphological change was seen after modifications as shown in Fig. 1C, D. The selected area electron diffraction (SAED) pattern of $\text{Ti}_3\text{C}_2@\text{TiO}_{2-x}$ (Fig. 1E, inset) indicated the crystalline nature of TiO_2 , whereas the lattice spacings of 0.352 nm were assigned to (101) plane of anatase TiO_2 [47]. Meanwhile, energy dispersive X-ray spectroscopy (EDS) indicated the presence of titanium, oxygen, and carbon elements in $\text{Ti}_3\text{C}_2@\text{TiO}_{2-x}$ (Fig. 1F, G and Additional file 1: Fig. S1A, B). Compared to Ti_3C_2 (20 nm), $\sim 40\text{--}80 \text{ nm}$ of height increases were noticed for $\text{Ti}_3\text{C}_2@\text{TiO}_2$ and $\text{Ti}_3\text{C}_2@\text{TiO}_{2-x}$, indicating in situ production and the decoration of TiO_2 onto Ti_3C_2 (Additional file 1: Fig. S2). The X-ray diffraction (XRD) spectrum of $\text{TiO}_{2-x}@\text{Ti}_3\text{C}_2$ was well-indexed



with TiO_2 (JCPDS no. 21–1272) and Ti_3C_2 (JCPDS no. 32–1383) as shown in Additional file 1: Fig. S3. The elemental composition and oxygen vacancies were

further confirmed by XPS spectroscopy. Additional file 1: Fig. S4A–E and Fig. 1H, I verified the presence of titanium (25.92%, 15.7%), oxygen (52.47%, 25.17%)

and carbon (21.62%, 44.74%) in $\text{Ti}_3\text{C}_2@\text{TiO}_{2-x}$ hybrid, respectively, while O 1 s peak is negatively shifted from 529.9 ($\text{Ti}_3\text{C}_2@\text{TiO}_2$) to 529.2 eV in $\text{Ti}_3\text{C}_2@\text{TiO}_{2-x}$ nanohybrid (Fig. 1H, I), which is attributed to the existence of oxygen vacancies within $\text{Ti}_3\text{C}_2@\text{TiO}_{2-x}$, favoring highly efficient ROS production [48, 49]. The quantitative analysis also indicated a prominent decrease in O/Ti ratio from 2 to 1.6 after reduction (Additional file 1: Fig. S4F), implying the creation of oxygen vacancies in $\text{Ti}_3\text{C}_2@\text{TiO}_{2-x}$. Such a thorough characterizations proved the successful fabrication of *in-situ* 2D $\text{Ti}_3\text{C}_2@\text{TiO}_{2-x}$ nanohybrid with desired oxygen deficiencies to accelerate ROS generation.

Later, $\text{Ti}_3\text{C}_2@\text{TiO}_{2-x}$ was surface functionalized with DSPE-PEG, which imparts an aqueous solubility and biocompatibility. Notably, the surface PEGylation did not induce any observable morphological change in the resultant TTP and $\text{Ti}_3\text{C}_2@\text{TiO}_2$ -PEG as shown in Additional file 1: Fig. S5A, B. FT-IR spectra of TTP showed the presence of $-\text{CH}_2$ and $\text{C}-\text{O}$ bonds at 2870 and 1100 cm^{-1} , respectively, which are assigned to the DSPE-PEG modification (Additional file 1: Fig. S6), while the amount of PEG loaded onto $\text{Ti}_3\text{C}_2@\text{TiO}_{2-x}$ hybrid was about 3% as quantitatively determined by TGA (Additional file 1: Fig. S7), indicating the successful surface grafting of $\text{Ti}_3\text{C}_2@\text{TiO}_{2-x}$ hybrid by PEG. The hydrodynamic diameter of TTP was about 170 nm as determined by DLS (Additional file 1: Fig. S8), whereas, the surface zeta potential of $\text{Ti}_3\text{C}_2@\text{TiO}_2$ -PEG and TTP was about -7.8 and -11.2 eV, respectively, suggesting limited protein binding and longer blood circulation (Additional file 1: Fig. S9) [50]. Owing to PEG grafting, TTP and $\text{Ti}_3\text{C}_2@\text{TiO}_2$ -PEG exhibited good stability in different physiological solutions such as PBS, Dulbecco's modified eagle medium (DMEM), and fetal bovine serum (FBS) as shown in Additional file 1: Fig. S10A, B. Meanwhile, no notable change was recorded in the hydrodynamic diameter of TTP and $\text{Ti}_3\text{C}_2@\text{TiO}_2$ -PEG under different physiological solutions for 3 days, verifying the excellent colloidal stability of TTP (Additional file 1: Fig. S10C, D). UV-vis/NIR absorption spectroscopy indicated the broadband absorption of TTP in NIR-II region without

any particular absorption peak (Fig. 1J), which is solely ascribed to the presence of 2D Ti_3C_2 sheets, suggesting the potential of as-designed TTP hybrid for dual-modal PT/PA imaging and PTT at second biowindow.

Evaluation of photothermal and sonodynamic capacity

Considering the good NIR-II absorption, the photothermal capacity of TTP was investigated. Figure 2A, B displayed significant temperature enhancement in TTP solution under 1064 nm laser irradiation (0.8 W/cm^2) for 5 min, which is directly proportional to the irradiation time and TTP concentration, respectively. Furthermore, the calculated photothermal conversion efficiency (PCE, η) of TTP was about 35.8% (Additional file 1: Fig. S11A, B) [51], which is superior or even comparable to many previously reported photothermal nanoagents [52–55]. Notably, under 5 repetitive laser on/off cycles, no apparent temperature decrease was recorded as shown in Additional file 1: Fig. S12A. Moreover, the absorption spectrum and TEM morphological characterization did not show any particular change in TTP even after 1064 nm laser irradiation for 20 min, suggesting the excellent photothermal stability of TTP (Additional file 1: Fig. S12B, C). Inorganic TiO_2 nanoparticles have been widely reported as sonosensitizers, capable of ROS production such as singlet oxygen ($^1\text{O}_2$) and hydroxyl radicals ($\cdot\text{OH}$), etc. under US irradiation [17, 18, 42, 56, 57]. Therefore, electron spin resonance (ESR) spectroscopy was employed to determine the ROS generation by TTP under US activation. Figure 2C presented the characteristic (1:1:1) peaks of $^1\text{O}_2$ after US stimulation of both $\text{Ti}_3\text{C}_2@\text{TiO}_2$ -PEG and TTP group, respectively. The $^1\text{O}_2$ generation ability of TTP was further evaluated by using 1, 3-diphenylisobenzofuran (DPBF) probe. Figure 2D and Additional file 1: Fig. S13 showed time-dependent gradual decrease in DPBF absorbance at 410 nm by both $\text{Ti}_3\text{C}_2@\text{TiO}_2$ -PEG and TTP group, while the control group did not reduce the DPBF absorbance at all. It is worth mentioning that TTP showed stronger $^1\text{O}_2$ production capacity than $\text{Ti}_3\text{C}_2@\text{TiO}_2$ -PEG, which is possibly ascribed to the presence of several oxygen vacancies within TiO_{2-x} . Notably, these oxygen vacancies

(See figure on next page.)

Fig. 2 **A** The real-time thermal images and **B** the corresponding heating curves of the varying concentrations of TTP aqueous solutions. **C** ESR spectra of $^1\text{O}_2$ /TEMP adduct by incubating $\text{Ti}_3\text{C}_2@\text{TiO}_2$ -PEG or TTP with TEMP (20 mM). **D** The absorbance profile of DPBF at 425 nm under different conditions and US stimulation (1 W/cm^2 , 1 MHz) for 5 min. **E** The absorbance spectra of DPBF treated with different concentrations (0–200 $\mu\text{g/mL}$) of TTP under US irradiation (1 W/cm^2 , 1 MHz, 5 min). **F** The absorbance spectra of DPBF treated with 50 $\mu\text{g/mL}$ of TTP under US irradiations with different power density (0– 1.6 W/cm^2 , 1 MHz, 5 min). **G** ESR spectra of $\cdot\text{OH}$ /DMPO adduct by incubating $\text{Ti}_3\text{C}_2@\text{TiO}_2$ -PEG or TTP with DMPO (10 mM). **H** The fluorescence intensity of NaOH solution (2 mM) containing TPA (0.5 mM) and treated with different concentrations of TTP, followed by US irradiation (1 W/cm^2 , 1 MHz, 3 min). **I** The fluorescence intensity of NaOH solution containing TPA (0.5 mM) and TTP (50 $\mu\text{g/mL}$) irradiated with US of different power density (0– 1.6 W/cm^2 , 1 MHz, 3 min). **J** Optical band gaps of TTP and TiO_2 . **K** Schematic illustration of the US-induced ROS generation by TTP hybrid, and the proposed mechanism of accelerated sonodynamic performance of TTP by enhanced separation of charge carriers through oxygen defects

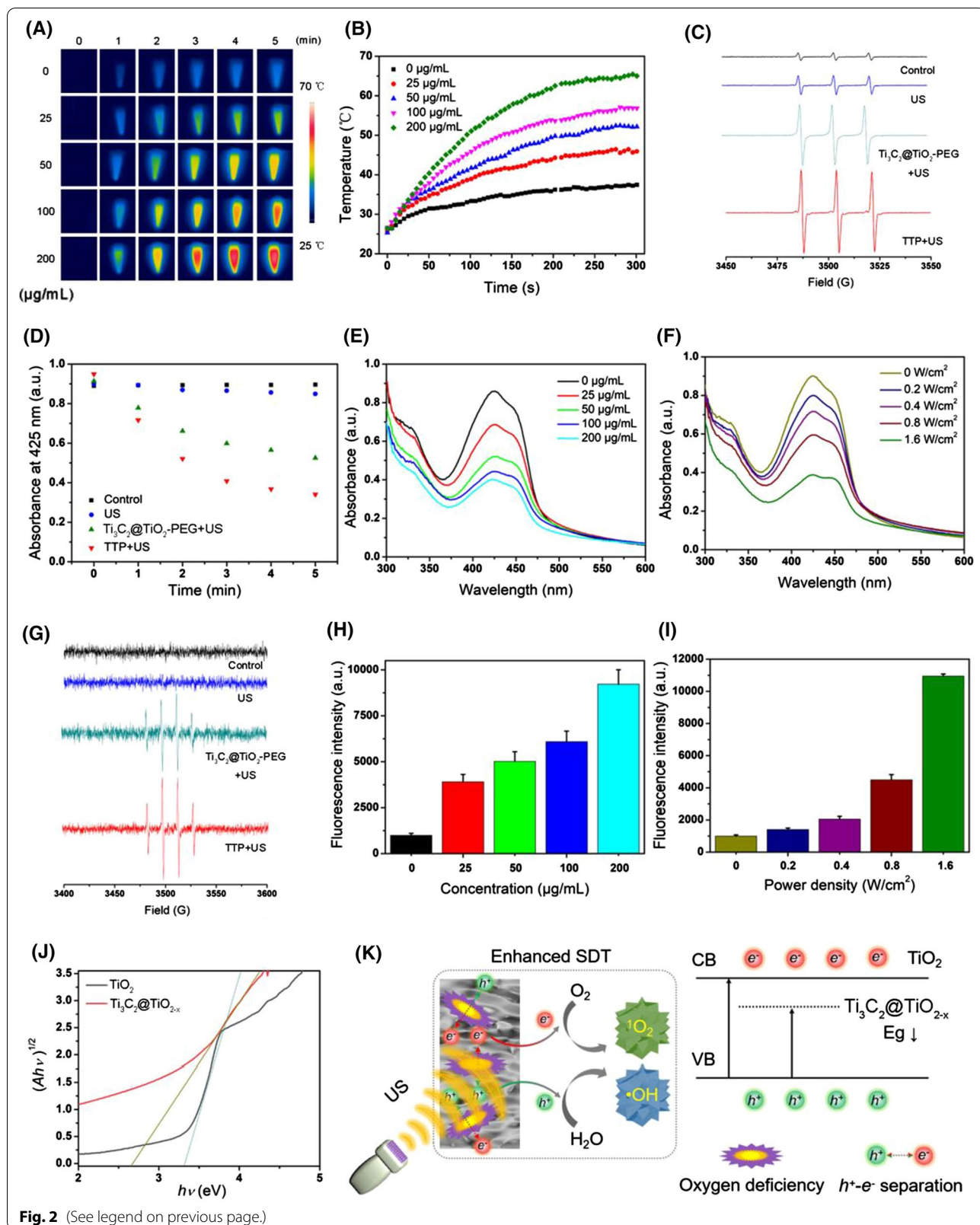


Fig. 2 (See legend on previous page.)

played a vital role as they promoted effective separation of charge carriers (electron–hole pairs), and thus facilitate an enhanced interaction between charge carriers and surface adsorbed oxygen molecules, leading to enhanced ROS generation. Meanwhile, the concentration and US power-dependent $^1\text{O}_2$ production was also recorded by TTP as shown in Fig. 2E, F and Additional file 1: Fig. S14A, B. Besides $^1\text{O}_2$, the characteristic (1:2:2:1) peaks of 5,5-Dimethyl-1-pyrroline N-oxide (DMPO) and $\cdot\text{OH}$ adducts were appeared both in $\text{TiO}_2@ \text{Ti}_3\text{C}_2\text{-PEG}$ and TTP groups, indicating the generation of $\cdot\text{OH}$ ions (Fig. 2G). Similarly, a $\cdot\text{OH}$ indicator TPA, which emits fluorescence after reacting with $\cdot\text{OH}$ under UV light, was also used to detect the ability of TTP to produce $\cdot\text{OH}$ under US stimulation. As shown in Additional file 1: Fig. S15, a strong fluorescence signal is generated at 422 nm after $\text{Ti}_3\text{C}_2@ \text{TiO}_2\text{-PEG}$ and TTP activation by US. However, the control group and US irradiation alone showed much weaker fluorescence signal. The quantitative analysis suggested that TTP has a stronger $\cdot\text{OH}$ production ability than $\text{Ti}_3\text{C}_2@ \text{TiO}_2\text{-PEG}$. Similar to $^1\text{O}_2$, the production of $\cdot\text{OH}$ is also dependent on TTP concentration and US power density (Fig. 2H, I). These results verified that TTP holds excellent $^1\text{O}_2$ and $\cdot\text{OH}$ production capacity under ultrasonic stimulation. For better apprehension of the sonodynamic performance of $\text{Ti}_3\text{C}_2@ \text{TiO}_{2-x}$, the band gap calculation was made by Kubelka–Munk function, which was about 3.32 and 2.65 eV for TiO_2 and $\text{Ti}_3\text{C}_2@ \text{TiO}_{2-x}$, respectively (Fig. 2J). Such a narrow band gap of $\text{Ti}_3\text{C}_2@ \text{TiO}_{2-x}$ than TiO_2 NPs could be ascribed to the overlapping oxygen deficiency induced defect states with the band edge of the semiconductor. Thereby, $\text{Ti}_3\text{C}_2@ \text{TiO}_{2-x}$ served as a charge trap, and remarkably restricts the charge recombination (electron–hole pairs) under US excitation, promoting an enhanced sonodynamic ROS generation during SDT (Fig. 2K).

In vitro combined PTT/SDT

The in vitro cellular uptake of TTP was determined by ICP-MS. The cellular uptake mechanism of TTP was investigated by using various inhibitors. As presented in Additional file 1: Fig. S16, the cellular uptake of TTP was significantly reduced when incubated with chlorpromazine or at 4 °C, suggesting that TTP entered into cells through an energy-dependent and clathrin-mediated endocytosis pathway. As shown in Fig. 3A, the Ti content in 4T1 cells increases gradually with an increase in incubation time, indicating an efficient cellular internalization of TTP. While, MTT assay revealed no potential cytotoxicity of internalized TTP on 4T1 and human embryonic kidney (HEK293T) cells in dark, suggesting good biocompatibility (Fig. 3B and Additional file 1: Fig. S17). However, TTP substantially reduced the cellular

viability of 4T1 cells under either 1064 nm laser (PTT) or US (SDT) activation, respectively. The cellular viability was reduced up to 45% and 39% by individual PTT and SDT treatment alone (Fig. 3C), whereas, the combined PTT/SDT triggered significant cellular killing, resulting in a dramatic decrease (16.5%) in cells viability, suggesting superior therapeutic killing performance of combined PTT/SDT treatment than either PTT or SDT alone. MTT findings were also further endorsed by live and dead assay (Fig. 3D) and Annexin V-FITC and PI staining (Fig. 3E) as much higher proportion of dead cells (apoptosis and necrosis) were observed after dual laser/US treatment (Additional file 1: Fig. S18), verifying an extensive in vitro cellular killing by synergistic PTT/SDT.

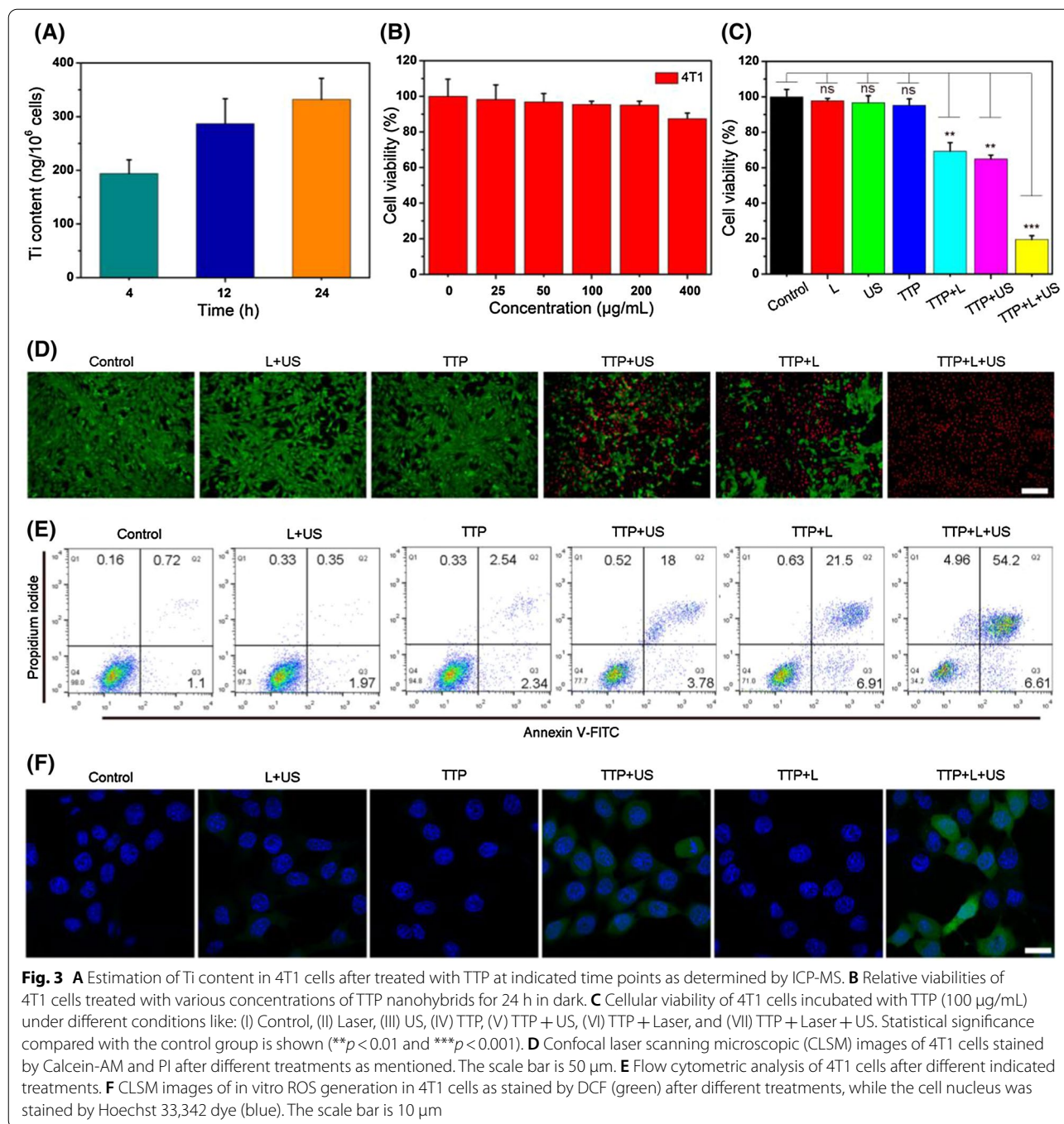
Considering that $^1\text{O}_2$ and $\cdot\text{OH}$ can be produced under ultrasonic stimulation in an aqueous solution. The ROS probe 2,7-dichlorofluorescein diacetate (DCFH-DA) was utilized to assess ROS production in vitro in 4T1 cells. Negligible green fluorescence was noticed in cells after treated with US, laser, or TTP alone, while an obvious green fluorescence was seen after simultaneous treatment with TTP and US (Fig. 3F), implying significant ROS production.

In vivo biocompatibility

Biosafety is an important prerequisite for the development of nanodrugs in biomedical field. Hence, the in vivo biocompatibility of TTP was evaluated by hemolysis assay, hematology analysis, and H&E staining of the major organs (heart, liver, spleen, lungs, and kidneys). Additional file 1: Fig. S19 showed no adverse effects of TTP on red blood cells, while all the hematological parameters, including liver (aspartate transaminase, AST, alanine aminotransferase, ALT), kidney function (blood urea nitrogen, BUN, creatinine, CRE), and other blood biochemical indicators as shown in Fig. 4A–E, were also in normal range like PBS-treated control mice. In addition, H&E analysis did not display any apparent inflammation in major organs (Fig. 4G). Moreover, like PBS-treated mice, no particular change was recorded in the body weight of TTP-treated mice even after one month (Additional file 1: Fig. S20). Collectively, these results verified the good biocompatibility and biosafety of TTP in vivo.

In vivo biodistribution and duplex PA/PT imaging

Prior to the determination of in vivo therapeutic potential of TTP, we assessed the in vivo biodistribution of TTP by PA imaging and ICP-MS, respectively. As expected, the PA signal intensity was positively correlated with the concentration of TTP (Additional file 1: Fig. S21). As can be seen in Fig. 5A, B, compared to pre-injection, the PA signal intensity is significantly enhanced in tumor tissues



after post-injection, indicating an effective tumor accumulation of TTP. Importantly, the highest PA signal was found at 4 h post-injection, which provides an effective guidance and optimal treatment time for tumor PTT in vivo. Next, the Ti content in major organs of mice

was detected by ICP-MS. Figure 5C displayed prominent accumulation of TTP in reticuloendothelial system e.g., liver and spleen, whereas, 5% ID/g of TTP was found in tumor tissues, which is advantageous for combined tumor PTT/SDT in vivo. Besides PA imaging

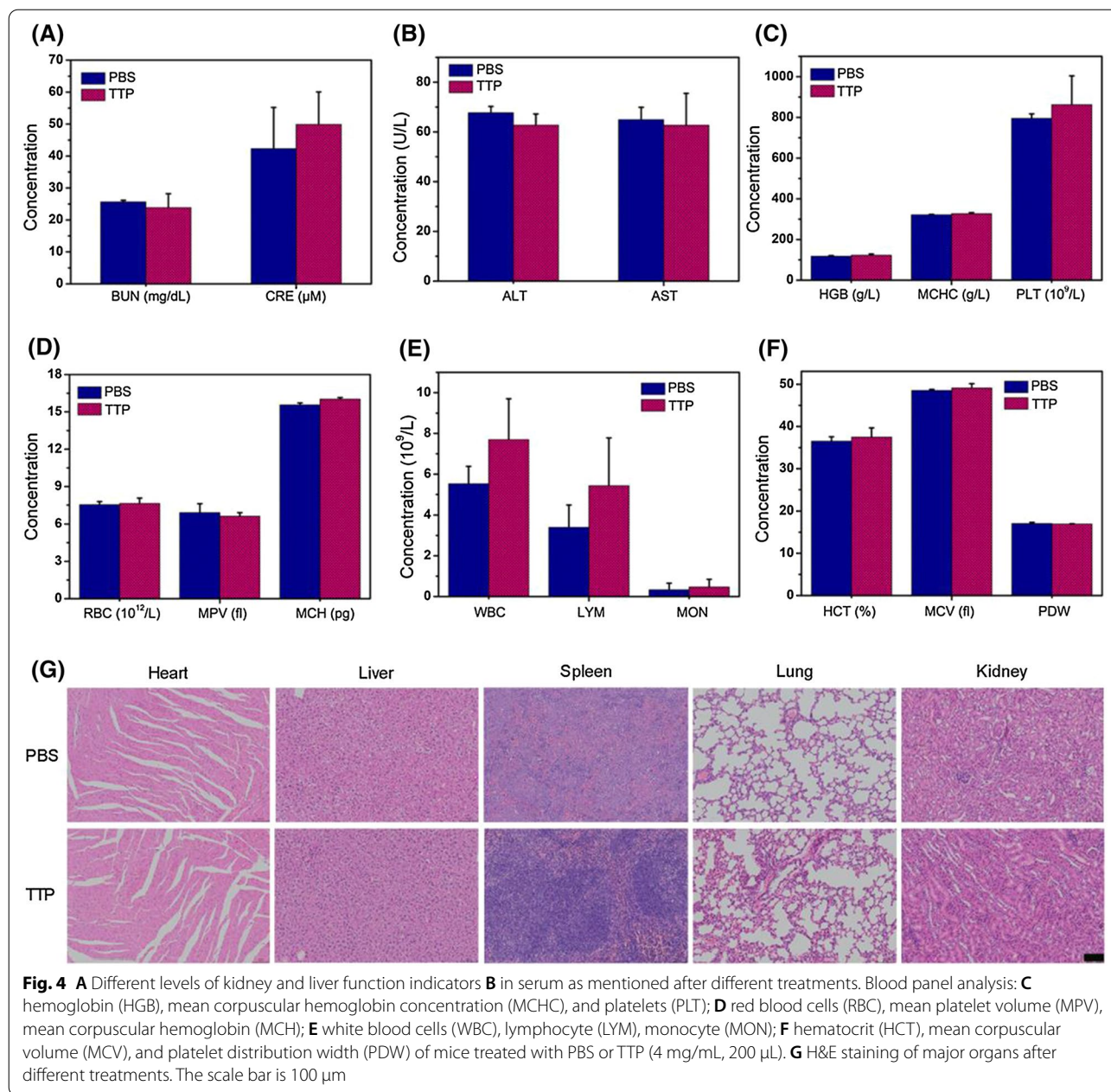
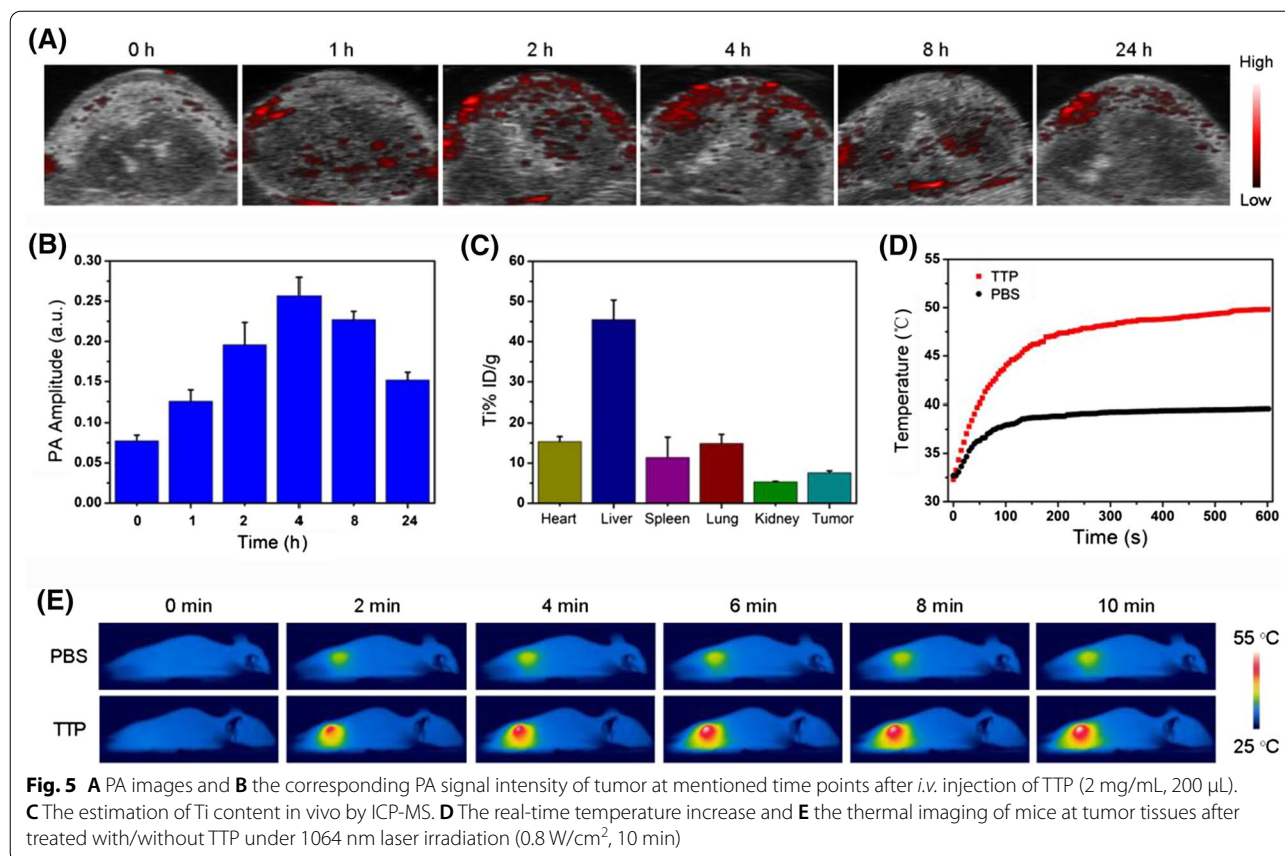


Fig. 4 **A** Different levels of kidney and liver function indicators **B** in serum as mentioned after different treatments. Blood panel analysis: **C** hemoglobin (HGB), mean corpuscular hemoglobin concentration (MCHC), and platelets (PLT); **D** red blood cells (RBC), mean platelet volume (MPV), mean corpuscular hemoglobin (MCH); **E** white blood cells (WBC), lymphocyte (LYM), monocyte (MON); **F** hematocrit (HCT), mean corpuscular volume (MCV), and platelet distribution width (PDW) of mice treated with PBS or TTP (4 mg/mL, 200 μL). **G** H&E staining of major organs after different treatments. The scale bar is 100 μm

and ICP-MS, in vivo PT imaging was also performed to determine the temperature enhancement at tumor site by intravenously injected TTP under 1064 nm laser excitation for 10 min. The temperature of TTP-treated mice was abruptly increased from 28 to 52 °C, while a slight temperature change was noticed in PBS group (Fig. 5D, E). These results demonstrated the good photothermal performance of TTP in vivo.

In vivo synergistic PTT/enhanced SDT

Finally, the therapeutic efficacy of synergistic PTT/enhanced SDT triggered by TTP was investigated. 4T1 tumor-bearing mice with a mean tumor volume of about 80 mm³ were randomly assigned to seven groups, and received an *i.v.* injection of either TTP (20 mg/kg) or PBS, respectively. The tumor volume of each mice undergo different treatment conditions, was recorded every two days, while after 14 days, all the tumors were dissected,

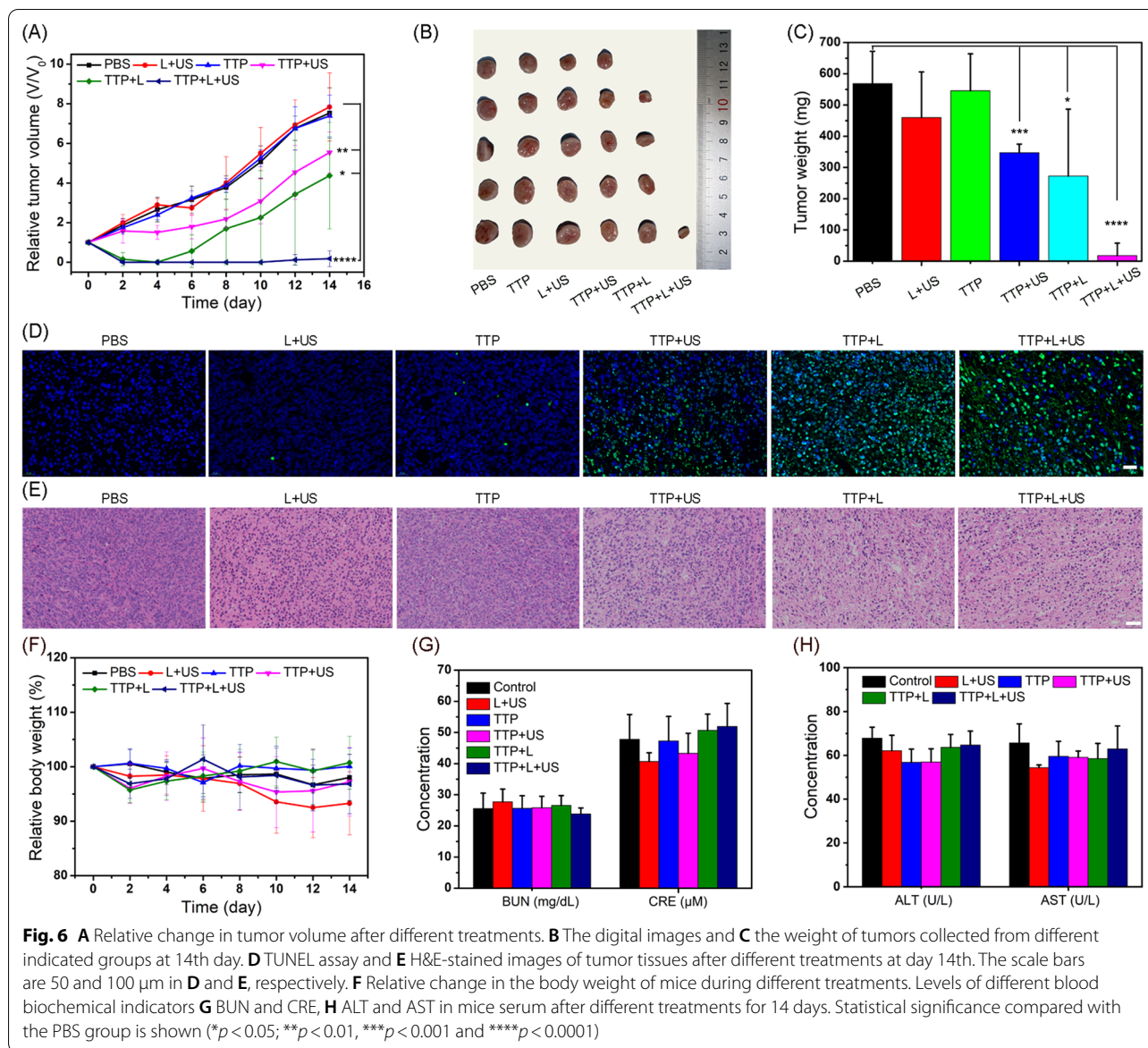


weighed, and photographed. As Additional file 1: d the tumor growth, whereas the combined PTT/SDT triggered complete tumor eradication. The *in vivo* therapeutic effects were further evaluated by TUNEL assay, which showed the highest green fluorescence intensity in the combined TPP + Laser + US treatment group (Fig. 6D), indicating substantial cellular apoptosis. Similarly, the H&E staining of tumor tissues verified the superior therapeutic effects as noticeable nuclear shrinkage and reduced number of cancer cells (Fig. 6E) were found in combined treatment than individual PTT or SDT alone. These results are in accordance with the *in vitro* findings. Remarkably, the body weight of the mice in each group was remained stable after different treatments (Fig. 6F). In addition, no significant lesions or damages were found in the major organs as confirmed by H&E staining (Additional file 1: Fig. S23) and blood biochemistry analysis (Fig. 6G, H), implying the negligible systemic toxicity of TTP *in vivo*.

Conclusion

In summary, TTP was prepared by the *in-situ* fabrication of ~ 10 nm TiO_{2-x} NPs with multiple oxygen defects onto the Ti₃C₂ nanosheets, followed by PEG grafting,

offering synergistic PTT/enhanced SDT under PA/PT bimodal imaging guidance in second biowindow. TTP possessed good colloidal stability, excellent photothermal conversion efficiency, and absorption in NIR-II region. Importantly, TTP with higher surface area and several oxygen-defects, facilitated higher surface adsorption of O₂ molecules as well as an efficient separation of charge carriers under US activation, promoting an enhanced interaction of charge carriers with surface adsorbed O₂ to trigger higher sonodynamic ROS generation than commonly reported TiO₂ NPs. Owing to good photothermal and enhanced US-stimulated ROS production capacity, TTP showed high therapeutic efficiency *in vitro* with appreciable biocompatibility, and demonstrated complete tumor elimination in 4T1 tumor bearing mice *in vivo*, because of synergistic photothermal enhanced SDT, which is far greater than single treatment modality. Our work demonstrated the design engineering of hybrid nanosystems for enhanced theranostics of deeply localized tumors in clinic.



Abbreviations

NIR-I: Near-infrared-I; ROS: Reactive oxygen species; PTT: Photothermal therapy; US: Ultrasound; SDT: Sonodynamic therapy; TiO_2 : Titanium dioxide; Ti_3C_2 : Titanium carbide; PA: Photoacoustic; PEG: Polyethylene glycol; TPAOH: Tetrapropylammonium hydroxide; DSPE-PEG: 1,2-Distearoyl-sn-glycero-3-phosphoethanolamine-N-[methoxy(polyethylene glycol)]; TPA: Terephthalic acid; MTT: 3-(4,5)-Dimethylthiazol-2-yl-5-(3,4-diphenyltetrazolium) bromide; PI: Propidium iodide; TEM: Transmission electron microscope; XPS: X-ray photoelectron spectrometer; FT-IR: Fourier transform infrared; TGA: Thermogravimetric analysis; DLS: Dynamic light scattering; ICP-MS: Inductively coupled plasma mass spectrometry; TTP: $\text{Ti}_3\text{C}_2@/\text{TiO}_2$ -PEG; PBS: Phosphate buffered saline; H&E: Hematoxylin and eosin; TUNEL: Terminal-deoxynucleotidyl transferase mediated nick end labeling; SAED: Selected area electron diffraction; EDS: Energy dispersive X-ray spectroscopy; XRD: X-ray diffraction; DMEM: Dulbecco's modified eagle medium; FBS: Fetal bovine serum; $^1\text{O}_2$: Singlet oxygen; $\cdot\text{OH}$: Hydroxyl radicals; ESR: Electron spin resonance; DPBF: 1,3-Diphenylisobenzofuran; DMPO: 5,5-Dimethyl-1-pyrroline N-oxide; HEK 293 T: Human embryonic kidney 293 T; DCFH-DA: 2,7-Dichlorofluorescein diacetate; AST: Aspartate transaminase; ALT: Alanine aminotransferase; BUN: Blood

urea nitrogen; CRE: Creatinine; HGB: Hemoglobin; MCHC: Mean corpuscular hemoglobin concentration; PLT: Platelets; RBC: Red blood cells; MPV: Mean platelet volume; MCH: Mean corpuscular hemoglobin; WBC: White blood cells; LYM: Lymphocyte; MON: Monocyte; HCT: Hematocrit; MCV: Mean corpuscular volume; PDW: Platelet distribution width; O_2 : Oxygen.

Supplementary Information

The online version contains supplementary material available at <https://doi.org/10.1186/s12951-022-01253-8>.

Additional file 1. Additional information includes part of material and methods, additional figures and tables.

Acknowledgements

This work is financially supported by National Key R&D Program of China (2018YFA0704000), National Natural Science Foundation of China

(82071985), Basic Research Program of Shenzhen (JCYJ20180507182413022, JCYJ20170412111100742), Guangdong Province Natural Science Foundation of Major Basic Research and Cultivation Project (2018B030308003), Shenzhen Science and Technology Program (KQTD20190929172538530) and the Fok Ying-Tong Education Foundation for Young Teachers in the Higher Education Institutions of China (161032). We thank Instrumental Analysis Center of Shenzhen University (Lihu Campus).

Authors' contributions

YZ, HL, and MRY: Investigation, Data curation, Writing—original draft. SL and YC: Writing—review & editing. JL & PH, Conceptualization, Supervision, Funding acquisition, Writing—review & editing. All authors read and approved the final manuscript.

Funding

This work is financially supported by Basic Research Program of Shenzhen (JCYJ20200109105620482, JCYJ20180507182413022), and Shenzhen Science and Technology Program (KQTD20190929172538530). We thank Instrumental Analysis Center of Shenzhen University (Lihu Campus).

Availability of data and materials

All data used to generate these results is available in the main text and supporting information.

Declarations

Ethics approval and consent to participate

All animal studies were approved by the Animal Ethics and Welfare Committee of Shenzhen University.

Consent for publication

All authors agree to be published.

Competing interests

The authors declare no conflict of interests.

Received: 30 October 2021 Accepted: 9 January 2022

Published online: 28 January 2022

References

- Miller KD, Nogueira L, Mariotto AB, Rowland JH, Yabroff KR, Alfano CM, Jemal A, Kramer JL, Siegel RL. Cancer treatment and survivorship statistics, 2019. *CA-Cancer J Clin.* 2019;69:363–85.
- Allen C, Her S, Jaffray DA. Radiotherapy for cancer: Present and future. *Adv Drug Deliv Rev.* 2017;109:1–2.
- Vasan N, Baselga J, Hyman DM. A view on drug resistance in cancer. *Nature.* 2019;575:299–309.
- Donaldson SS, Lenon RA, Donaldson SS. Alterations of nutritional status. Impact of chemotherapy and radiation therapy. *Cancer.* 2015;43:2036–52.
- Soussain C, Ricard DD, Fike JR, Mazon JJ, Delattre JY. CNS complications of radiotherapy and chemotherapy. *Lancet.* 2009;374:1639–51.
- Tohme S, Simmons RL, Tsung A. Surgery for cancer: A trigger for metastases. *Cancer Res.* 2017;77:1548–52.
- Wang X, Zhong X, Gong F, Chao Y, Cheng L. Newly developed strategies for improving sonodynamic therapy. *Mater Horiz.* 2020;7:2028–46.
- Gong F, Cheng L, Yang N, Gong Y, Ni Y, Bai S, Wang X, Chen M, Chen Q, Liu Z. Preparation of TiH_{1.924} nanodots by liquid-phase exfoliation for enhanced sonodynamic cancer therapy. *Nat Commun.* 2020;11:3712.
- Qian X, Zheng Y, Chen Y. Micro/nanoparticle-augmented sonodynamic therapy (SDT): Breaking the depth shallow of photoactivation. *Adv Mater.* 2016;28:8097–129.
- Fei G, Liang, Cheng, Nailin, Yang, Oshra, Betzer, Liangzhu, Feng: Ultrasmall oxygen-deficient bimetallic oxide MnWO₄ nanoparticles for depletion of endogenous GSH and enhanced sonodynamic cancer therapy. *Adv Mater.* 2019;31:1900730.
- Huang P, Qian X, Chen Y, Yu L, Lin H, Wang L, Zhu Y, Shi J. Metalloporphyrin-encapsulated biodegradable nanosystems for highly efficient magnetic resonance imaging-guided sonodynamic cancer therapy. *J Am Chem Soc.* 2017;139:1275–84.
- Pang X, Xu C, Jiang Y, Xiao Q, Leung AW. Natural products in the discovery of novel sonosensitizers. *Pharmacol Ther.* 2016;162:144–51.
- Lin H, Li S, Wang J, Chu C, Zhang Y, Pang X, Lv P, Wang X, Zhao Q, Chen J, et al. A single-step multi-level supramolecular system for cancer sonotheranostics. *Nanoscale Horiz.* 2019;4:190–5.
- Murdoch M, Waterhouse GIN, Nadeem MA, Metson JB, Keane MA, Howe RF, Llorca J, Idriss H. The effect of gold loading and particle size on photocatalytic hydrogen production from ethanol over Au/TiO₂ nanoparticles. *Nat Chem.* 2011;3:489–92.
- Han X, Huang J, Jing X, Yang D, Lin H, Wang Z, Li P, Chen Y. Oxygen-deficient black titania for synergistic/enhanced sonodynamic and photoinduced cancer therapy at near infrared-II biowindow. *ACS Nano.* 2018;12:4545–55.
- Wang X, Zhong X, Bai L, Xu J, Cheng L. Ultrafine titanium monoxide (TiO_{1+x}) nanorods for enhanced sonodynamic therapy. *J Am Chem Soc.* 2020;142:6527–37.
- Deepagan VG, You DG, Um W, Ko H, Kwon S, Choi KY, Yi G-R, Lee JY, Lee DS, Kim K, et al. Long-circulating Au-TiO₂ nanocomposite as a sonosensitizer for ROS-mediated eradication of cancer. *Nano Lett.* 2016;16:6257–64.
- Cao Y, Wu T, Dai W, Dong H, Zhang X. TiO₂ nanosheets with Au nanocrystals decorated edge for mitochondria-targeting enhanced sonodynamic therapy. *Chem Mater.* 2019;31:9105–14.
- Zhang DY, Zheng Y, Zhang H, Sun JH, Tan CP, He L, Zhang W, Ji LN, Mao ZW. Delivery of phosphorescent anticancer iridium (III) complexes by polydopamine nanoparticles for targeted combined photothermal-chemotherapy and thermal/photoacoustic/lifetime imaging. *Adv Sci.* 2018;5:1800581.
- Wang S, Lin J, Wang Z, Zhou Z, Bai R, Lu N, Liu Y, Fu X, Jacobson O, Fan W, et al. Core-satellite polydopamine-gadolinium-metallofullerene nanotheranostics for multimodal imaging guided combination cancer therapy. *Adv Mater.* 2017;29:1701013.
- Zhang DY, Xu H, He T, Younis MR, Zeng L, Liu H, et al. Cobalt carbide-based theranostic agents for in vivo multimodal imaging guided photothermal therapy. *Nanoscale.* 2020;12:7174–9.
- Chen Y, Li ZH, Pan P, Hu JJ, Cheng SX, Zhang XZ. Tumor-microenvironment-triggered ion exchange of a metal-organic framework hybrid for multimodal imaging and synergistic therapy of tumors. *Adv Mater.* 2020;32:2001452.
- Sun W, Du Y, Liang X, Yu C, Fang J, Lu W, Guo X, Tian J, Jin Y, Zheng J. Synergistic triple-combination therapy with hyaluronic acid-shelled PPy/CPT nanoparticles results in tumor regression and prevents tumor recurrence and metastasis in 4T1 breast cancer. *Biomaterials.* 2019;217:119264.
- Younis MR, Wang C, An R, Wang S, Younis MA, Li Z-Q, Wang Y, Ihsan A, Ye D, Xia X-H. Low power single laser activated synergistic cancer phototherapy using photosensitizer functionalized dual plasmonic photothermal nanoagents. *ACS Nano.* 2019;13:2544–57.
- Fu L-H, Qi C, Hu Y-R, Lin J, Huang P. Glucose oxidase-instructed multimodal synergistic cancer therapy. *Adv Mater.* 2019;31:1808325.
- He T, Yuan Y, Jiang C, Blum NT, He J, Huang P, Lin J. Light-triggered transformable ferrous ion delivery system for photothermal primed chemodynamic therapy. *Angew Chem Int Ed.* 2021;60:6047–54.
- Yang C, Younis MR, Zhang J, Qu J, Lin J, Huang P. Programmable NIR-II photothermal-enhanced starvation-primed chemodynamic therapy using glucose oxidase-functionalized ancient pigment nanosheets. *Small.* 2020;16:2001518.
- Zhang Y, Song T, Feng T, Wan Y, Blum NT, Liu C, Zheng C, Zhao Z, Jiang T, Wang J, et al. Plasmonic modulation of gold nanotheranostics for targeted NIR-II photothermal-augmented immunotherapy. *Nano Today.* 2020;35:100987.
- Tian B, Wang C, Zhang S, Feng L, Liu Z. Photothermally enhanced photodynamic therapy delivered by nano-graphene oxide. *ACS Nano.* 2011;5:7000–9.
- Zhang DY, Zheng Y, Tan CP, Sun JH, Zhang W, Ji LN, Mao ZW. Graphene oxide decorated with Ru(II)-polyethylene glycol complex for lysosome-targeted imaging and photodynamic/photothermal therapy. *ACS Appl Mater Interfaces.* 2017;9:6761–71.
- Liang S, Deng X, Chang Y, Sun C, Lin J. Intelligent hollow Pt-CuS janus architecture for synergistic catalysis-enhanced sonodynamic and photothermal cancer therapy. *Nano Lett.* 2019;19:4134–45.

32. Li C-Q, Zhao D-H, Hou X-L, Zhang B, Song L-B, Jin R-M, Zhao Y-D, Liu BL. *In situ* synthesis of multifunctional tellurium nanorods stabilized by polypeptide-engineered for photothermal-sonodynamic combination therapy of tumors. *Chem Eng J*. 2021;417:127989.
33. Lin H, Wang Y, Gao S, Chen Y, Shi J. Theranostic 2D tantalum carbide (MXene). *Adv Mater*. 2018;30:1703284.
34. He W, Ai K, Jiang C, Li Y, Song X, Lu L. Plasmonic titanium nitride nanoparticles for *in vivo* photoacoustic tomography imaging and photothermal cancer therapy. *Biomaterials*. 2017;132:37–47.
35. Kumar S, Lei Y, Alshareef NH, Quevedo-Lopez MA, Salama KN. Biofunctionalized two-dimensional Ti_3C_2 MXenes for ultrasensitive detection of cancer biomarker. *Biosens Bioelectron*. 2018;121:243–9.
36. Dai C, Lin H, Xu G, Liu Z, Wu R, Chen Y. Biocompatible 2D titanium carbide (MXenes) composite nanosheets for pH-responsive MRI-guided tumor hyperthermia. *Chem Mater*. 2017;29:8637–52.
37. Yu X, Cai X, Cui H, Lee S-W, Yu X-F, Liu B. Fluorine-free preparation of titanium carbide MXene quantum dots with high near-infrared photothermal performances for cancer therapy. *Nanoscale*. 2017;9:17859–64.
38. Zhou B, Yin H, Dong C, Sun L, Feng W. Biodegradable and excretable 2D W_133C i-MXene with vacancy ordering for theory-oriented cancer nanotheranostics in near-infrared biowindow. *Adv Sci*. 2021;1:2101043.
39. Huang H, Feng W, Chen Y. Two-dimensional biomaterials: material science, biological effect and biomedical engineering applications. *Chem Soc Rev*. 2021;50:11381–485.
40. Feng W, Wang R, Zhou Y, Ding L, Gao X. Ultrathin molybdenum carbide MXene with fast biodegradability for highly efficient theory-oriented photonic tumor hyperthermia. *Adv Funct Mater*. 2019;29:1901942.
41. Mao C, Zuo F, Hou Y, Bu X, Feng P. *In situ* preparation of a Ti^{3+} self-doped TiO_2 film with enhanced activity as photoanode by N_2H_4 reduction. *Angew Chem Int Ed*. 2014, 53: 10485–9.
42. Shi J, Chen Z, Wang B, Wang L, Lu T, Zhang Z. Reactive oxygen species-manipulated drug release from a smart envelope-type mesoporous titanium nanovehicle for tumor sonodynamic-chemotherapy. *ACS Appl Mater Interfaces*. 2015;7:28554–65.
43. Wang M, Hou Z, Liu S, Liang S, Ding B, Zhao Y, Chang M, Han G, Kheraif AAA, Lin J. A multifunctional nanovaccine based on *L*-arginine-loaded black mesoporous titania: Ultrasound-triggered synergistic cancer sonodynamic therapy/gas therapy/immunotherapy with remarkably enhanced efficacy. *Small*. 2021;17:2005728.
44. Su K, Tan L, Liu X, Cui Z, Zheng Y, Li B, Han Y, Li Z, Zhu S, Liang Y, et al. Rapid photo-sonotherapy for clinical treatment of bacterial infected bone implants by creating oxygen deficiency using sulfur doping. *ACS Nano*. 2020;14:2077–89.
45. Liu C, Kong D, Hsu P-C, Yuan H, Lee H-W, Liu Y, Wang H, Wang S, Yan K, Lin D, et al. Rapid water disinfection using vertically aligned MoS_2 nanofilms and visible light. *Nat Nanotechnol*. 2016;11:1098–104.
46. Yang C, Liu Y, Sun X, Zhang Y, Hou L, Zhang Q, Yuan C. *In-situ* construction of hierarchical accordion-like TiO_2/Ti_3C_2 nanohybrid as anode material for lithium and sodium ion batteries. *Electrochim Acta*. 2018;271:165–72.
47. Ren Y, Hardwick LJ, Bruce PG. Lithium intercalation into mesoporous anatase with an ordered 3D pore structure. *Angew Chem Int Ed*. 2010;122:2624–8.
48. Wang Z, Yang C, Lin T, Yin H, Chen P, Wan D, Xu F, Huang F, Lin J, Xie X. Visible-light photocatalytic, solar thermal and photoelectrochemical properties of aluminium-reduced black titania. *Energy Environ Sci*. 2013;6:3007–14.
49. Lin T, Yang C, Wang Z, Yin H, Lü X, Huang F, Lin J, Xie X, Jiang M. Effective nonmetal incorporation in black titania with enhanced solar energy utilization. *Energy Environ Sci*. 2014;7:967–72.
50. Suk JS, Xu Q, Kim N, Hanes J, Ensign LM. PEGylation as a strategy for improving nanoparticle-based drug and gene delivery. *Adv Drug Deliv Rev*. 2016;99:28–51.
51. Zhang D-Y, Zheng Y, Zhang H, Yang G-G, Tan C-P, He L, Ji L-N, Mao Z-W. Folate receptor-targeted theranostic IrS_x nanoparticles for multimodal imaging-guided combined chemo-photothermal therapy. *Nanoscale*. 2018;10:22252–62.
52. Yang T, Tang Ya, Liu L, Lv X, Wang Q, Ke H, Deng Y, Yang H, Yang X, Liu G. Size-dependent Ag_2S nanodots for second near-infrared fluorescence/photoacoustics imaging and simultaneous photothermal therapy. *ACS Nano*. 2017;11:1848–57.
53. Hessel CM, Pattani VP, Rasch M, Panthani MG, Koo B, Tunnell JW, Korgel BA. Copper selenide nanocrystals for photothermal therapy. *Nano Lett*. 2011;11:2560–6.
54. Tian Q, Jiang F, Zou R, Liu Q, Hu J. Hydrophilic Cu_9S_8 nanocrystals: a photothermal agent with a 25.7% heat conversion efficiency for photothermal ablation of cancer cells *in vivo*. *ACS Nano*. 2011;1(5):9761.
55. Tian Q, Hu J, Zhu Y, Zou R, Chen Z, Yang S, Li R, Su Q, Han Y, Liu X. Sub-10 nm $Fe_3O_4@Cu_{2-x}S$ core-shell nanoparticles for dual-modal imaging and photothermal therapy. *J Am Chem Soc*. 2013;135:8571–7.
56. Lin X, Liu S, Zhang X, Zhu R, Chen S, Chen X, Song J, Yang H. An ultrasound activated vesicle of janus Au-MnO nanoparticles for promoted tumor penetration and sono-chemodynamic therapy of orthotopic liver cancer. *Angew Chem Int Ed*. 2020;59:1682–8.
57. Bai S, Yang N, Wang X, Gong F, Dong Z, Gong Y, Liu Z, Cheng L. Ultrasmall iron-doped titanium oxide nanodots for enhanced sonodynamic and chemodynamic cancer therapy. *ACS Nano*. 2020;14:15119–30.

Publisher's Note

Springer Nature remains neutral with regard to jurisdictional claims in published maps and institutional affiliations.

Ready to submit your research? Choose BMC and benefit from:

- fast, convenient online submission
- thorough peer review by experienced researchers in your field
- rapid publication on acceptance
- support for research data, including large and complex data types
- gold Open Access which fosters wider collaboration and increased citations
- maximum visibility for your research: over 100M website views per year

At BMC, research is always in progress.

Learn more biomedcentral.com/submissions

